Supplementary Information

Discovery of oxide Li-conducting electrolytes with corner-sharing frameworks via topology-constrained crystal structure prediction

Seungwoo Hwang[a], Jiho Lee[a], Jisu Kim[a], Seungwu Han[a,b], Youngho Kang[c*], and Sungwoo Kang[d,e*]

[a]*Department of Materials Science and Engineering, Seoul National University, Seoul, 08826, Republic of Korea*
[b]*AI center, Korea Institute for Advanced Study, Seoul, 02455, Republic of Korea*
[c]*Department of Materials Science and Engineering, Incheon National University, Incheon, 22012, Republic of Korea*
[d]*Computational Science Research Center, Korea Institute of Science and Technology (KIST), Seoul, 02792, Republic of Korea*
[e]*Division of Nanoscience and Technology, KIST School, University of Science and Technology (UST), Seoul, 02792, Republic of Korea*

[*] Corresponding authors: youngho84@inu.ac.kr, sung.w.kang@kist.re.kr

Supplementary Note 1. Benchmark test of TOPIC against existing CSP methods

To evaluate the search efficiency of TOPIC, we performed benchmark tests against existing crystal structure prediction approaches.

Comparison with SPINNER

We first compare TOPIC with SPINNER,[1,2] an MLIP-accelerated evolutionary CSP method without explicit topology constraints. For a fair comparison, structure generation is carried out using the same distance constraints (minimum interatomic distance in melt-quench molecular dynamics simulation trajectory) and the same MLIPs. As benchmark systems, we select five compounds, $LiTi_2P_3O_{12}$, $LiGaSe_2O_6$, $LiTiPO_5$, $LiTaSiO_5$, and β-$LiAlSiO_4$, for which TOPIC is able to identify the reference framework within 60,000 generated structures. For each system, 60,000 structures are generated with SPINNER, and the number of times the reference framework was identified (N_{found}) and the total wall time are compared. All calculations are performed on the same 32-core CPU, and the reported wall times correspond to the total elapsed time using those 32 cores.

The results are summarized in Table S2. For SPINNER, predictions are performed for both Li-removed framework structures and all-atom structures, using MLIPs trained on the Li-removed dataset and the all-atom dataset, respectively. In all benchmark systems, TOPIC identifies the reference framework more frequently than SPINNER. The N_{found} values obtained with TOPIC are substantially higher than those obtained with SPINNER, and in some cases, SPINNER does not identify the reference structure within the 60,000 generated structures. TOPIC also requires shorter wall time than SPINNER. This efficiency gain arises because, in TOPIC, structures that do not satisfy the corner-sharing framework condition after the Lennard-Jones-based pre-relaxation step are discarded before further relaxation, thereby avoiding unnecessary computation for irrelevant candidates. We also note that SPINNER applied to Li-removed frameworks is more efficient than SPINNER applied to all-atom structures, which further supports the effectiveness of the strategy of TOPIC.

Comparison with MAGUS

We next compare TOPIC with MAGUS,[3] a previously reported constrained CSP method based on symmetry principles that showed the highest efficiency in benchmark tests. For this comparison, we use a published benchmark example from the previous work,[3] $Mg_3Al_2Si_3O_{12}$, whose framework can be regarded as corner-sharing when Mg atoms are excluded.

Using an MLIP trained in the same manner as described in the main text, except that Mg atoms rather than Li atoms are excluded during training, we carry out CSP with TOPIC using 60,000 generated structures. In this benchmark, TOPIC identifies the reference structure approximately once every 28 generated structures, whereas the published MAGUS result identified it approximately once every 125 generated structures. This comparison indicates that TOPIC can achieve substantially higher search efficiency when the target topology is well constrained. However, we note that differences in distance constraints and other implementation details may also affect the results.

Supplementary Figures.

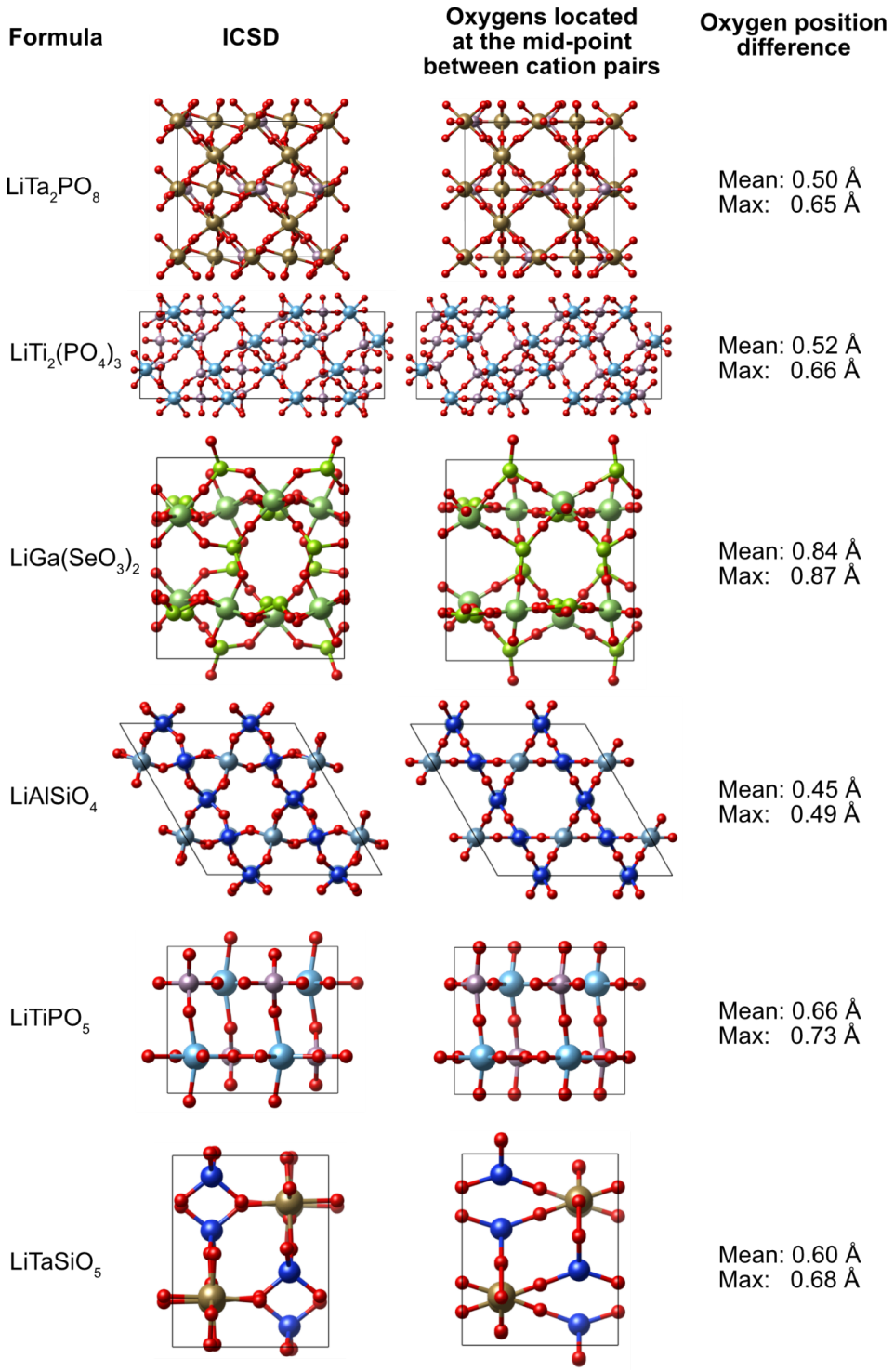

Fig. S1. Validation of O-atom placement at cation–cation midpoints. Framework structures are shown for experimentally reported reference compounds (ICSD)[4] and for corresponding models with the same cation sublattice, where O atoms were constrained to the midpoints of cation pairs. The mean and maximum deviations of O-atom positions from the ICSD references are indicated at right. In all cases, O atoms constrained to midpoints remain close to their experimental positions, with no deviation exceeding 1 Å.

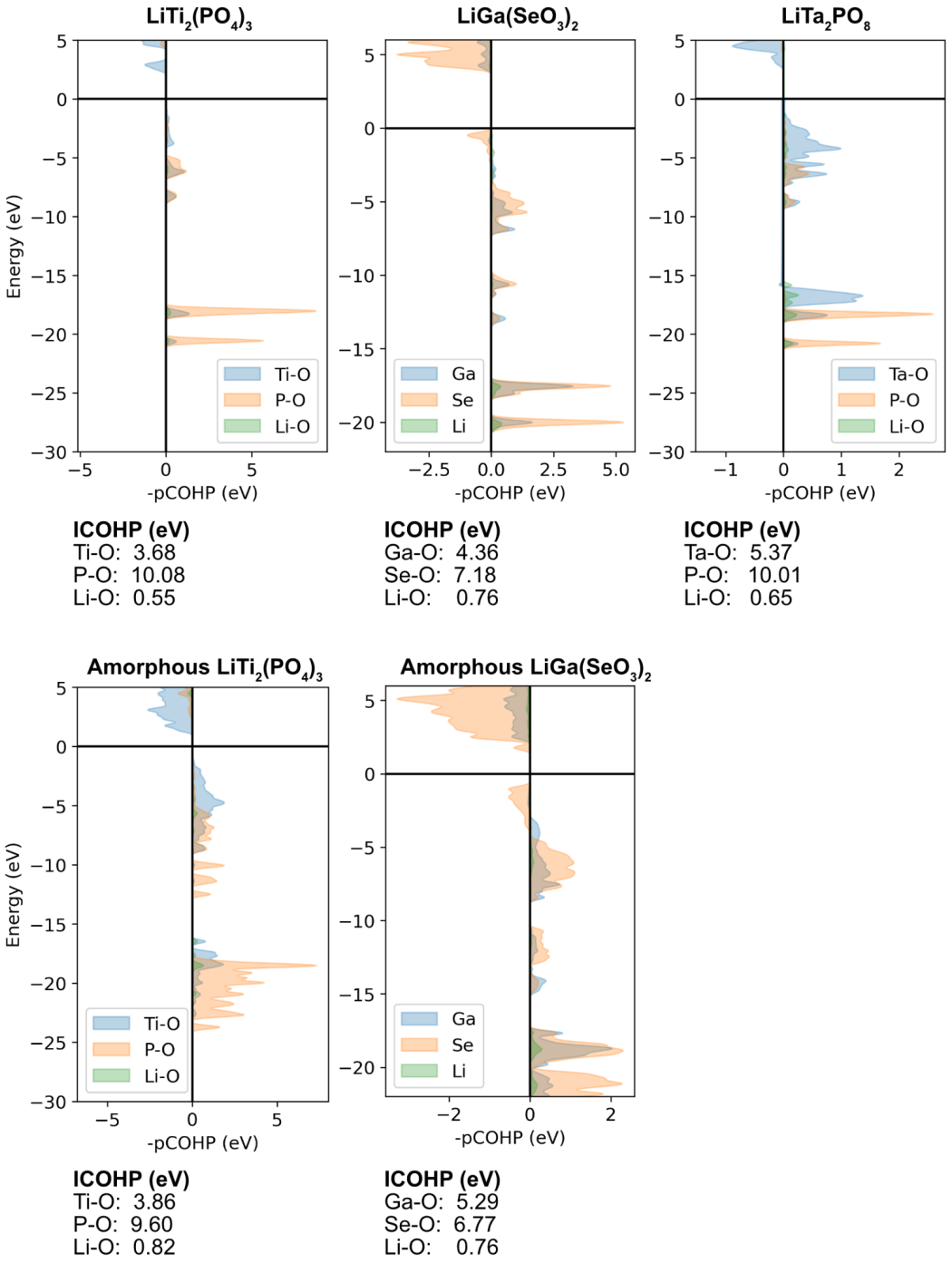

Fig. S2. Crystal orbital Hamilton population (COHP) analysis[5] of validation systems. Top panels: COHP plots for crystalline $LiTi_2(PO_4)_3$, $LiGa(SeO_3)_2$, and $LiTa_2PO_8$, resolved into framework cation–O and Li–O contributions. Bottom panels: corresponding COHP analyses for their melt-quenched amorphous phases. For each case, the integrated COHP (ICOHP) values, reported below the plots, quantify bond strength. Across both crystalline and amorphous systems, Li–O interactions are consistently the weakest compared with framework cation–O bonds, confirming the minor structural role of Li.

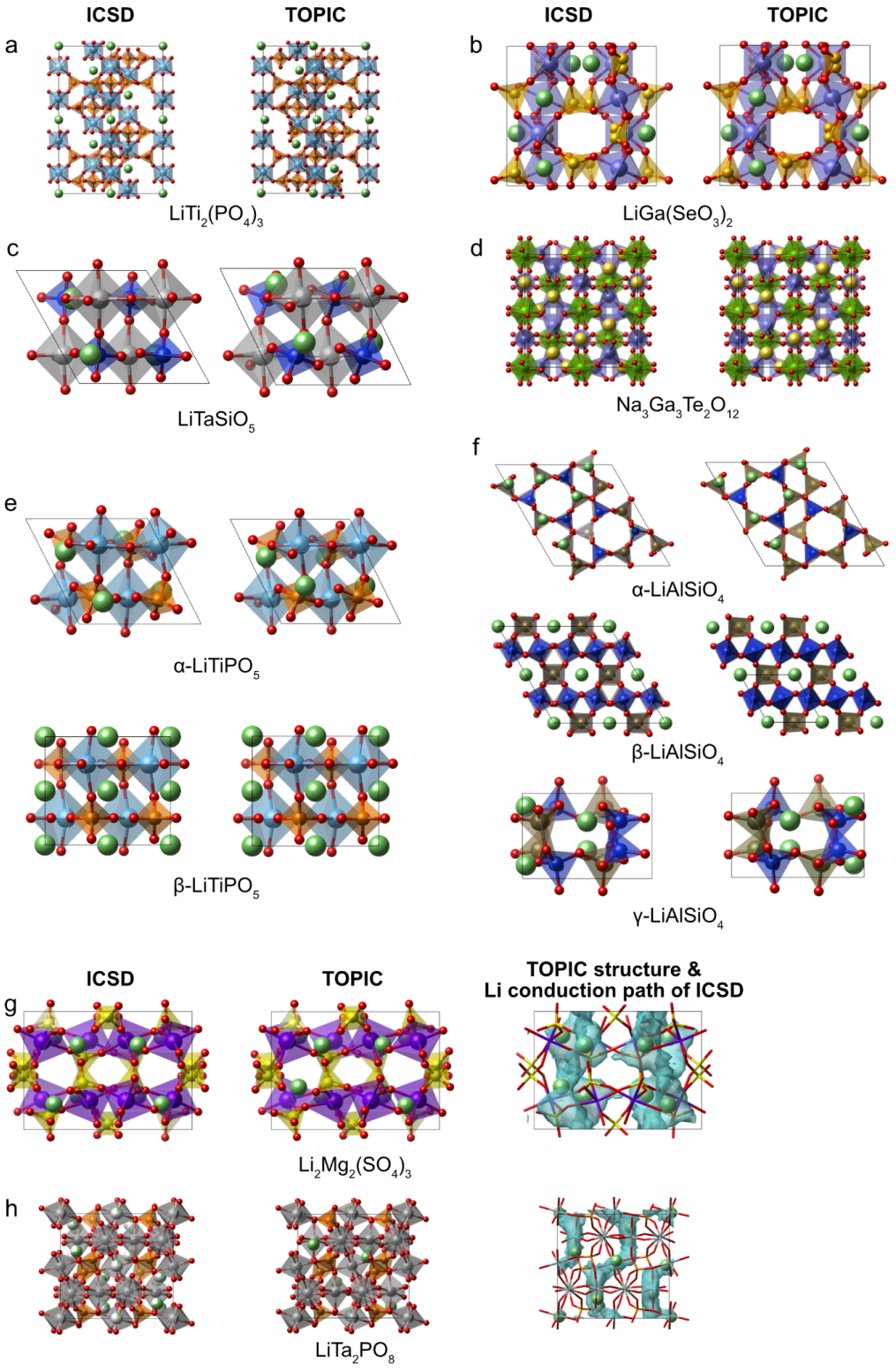

Fig. S3. Comparison of TOPIC-predicted structures with experimentally reported reference structures. For each system, the reference (ICSD) structure is shown alongside the corresponding TOPIC prediction. Among ten target compounds with ordered Li sites, TOPIC reproduces six with the correct Li positions ($LiTi_2(PO_4)_3$, $LiGa(SeO_3)_2$, $Na_3Ga_3Te_2O_{12}$, β-$LiTiPO_5$, α-$LiAlSiO_4$, and β-$LiAlSiO_4$), while the remaining cases preserve the correct polyhedral connectivity with minor distortions ($LiTaSiO_5$, α-$LiTiPO_5$, and γ-$LiAlSiO_4$) or deviations in Li sites ($Li_2Mg_2(SO_4)_3$). For (g) $Li_2Mg_2(SO_4)_3$ and (h) $LiTa_2PO_8$, Li conduction pathways obtained from molecular dynamics simulations initialized from the ICSD structures are overlaid on the TOPIC-predicted structures, confirming that predicted Li sites fall within established transport channels.

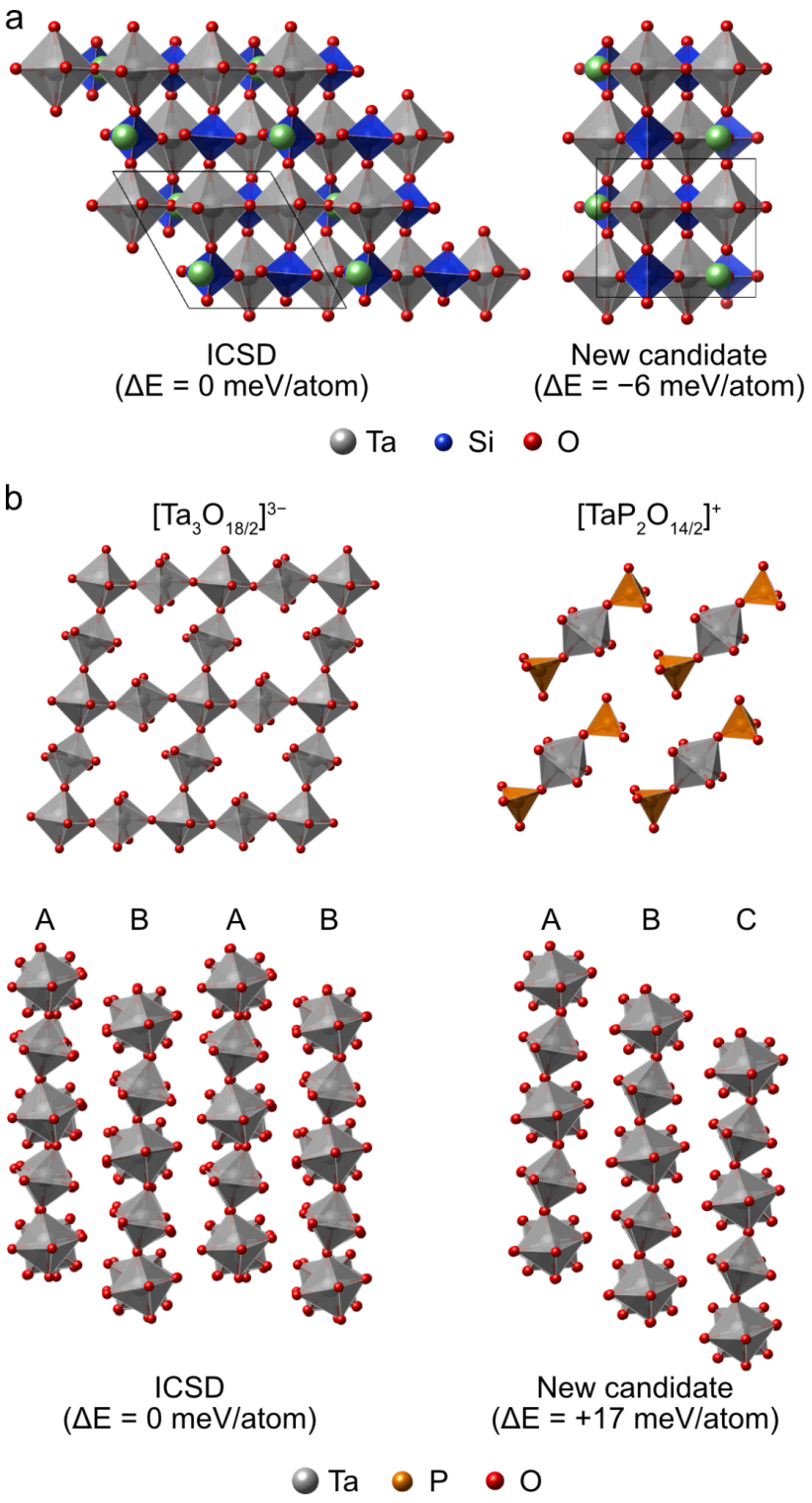

Fig. S4. Unreported low-energy structures in validation systems predicted by TOPIC. (a) Comparison between the ICSD reference structure and the TOPIC-identified structure of the $LiTaSiO_5$ system. The predicted phase, distinguished by a different stacking sequence, is 6 meV atom^{-1} lower in energy than the reported structure. (b) Predicted metastable polymorph of $LiTa_2PO_8$, lying 17 meV atom^{-1} above the reported phase. Top: polyhedral motifs—$[Ta_3O_{18/2}]^{3-}$ and $[TaP_2O_{14/2}]^{+}$—as described in Ref.[6] for the known structure. Bottom: stacking sequence of the $[Ta_3O_{18/2}]^{3-}$ motif in both the ICSD and TOPIC-predicted structures, together with their relative energies.

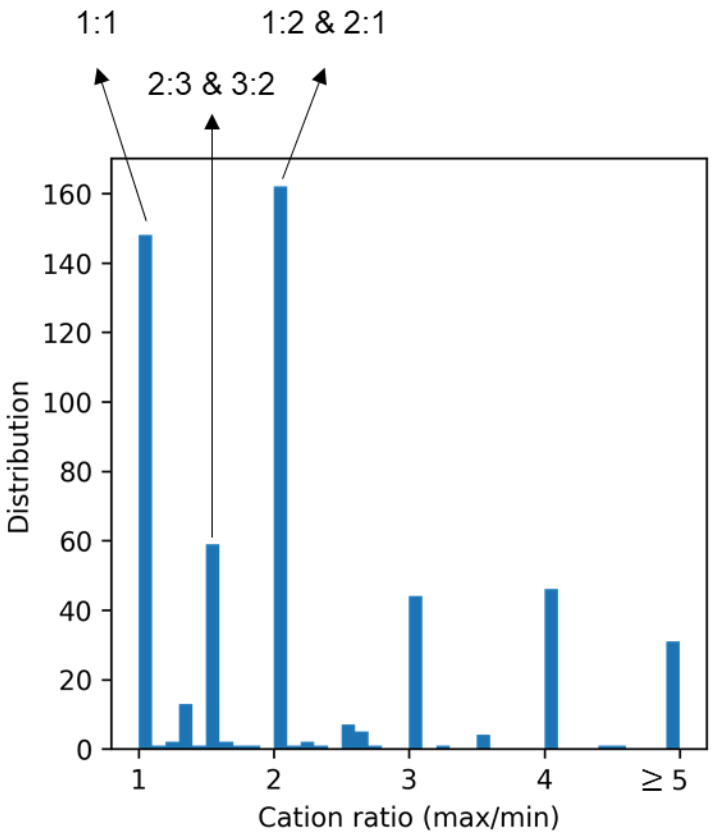

Fig. S5. Distribution of cation ratios in experimentally reported Li-containing quaternary oxides. The cation ratio is defined as the maximum number of cations divided by the minimum number of cations in a given composition (excluding Li), based on entries from the Materials Project database.[7] The most frequently observed ratios are 1:1, 2:1 (and its inverse 1:2), and 3:2 (and its inverse 2:3), which are highlighted in the plot. These ratios form the basis for selecting candidate compositions explored in this work.

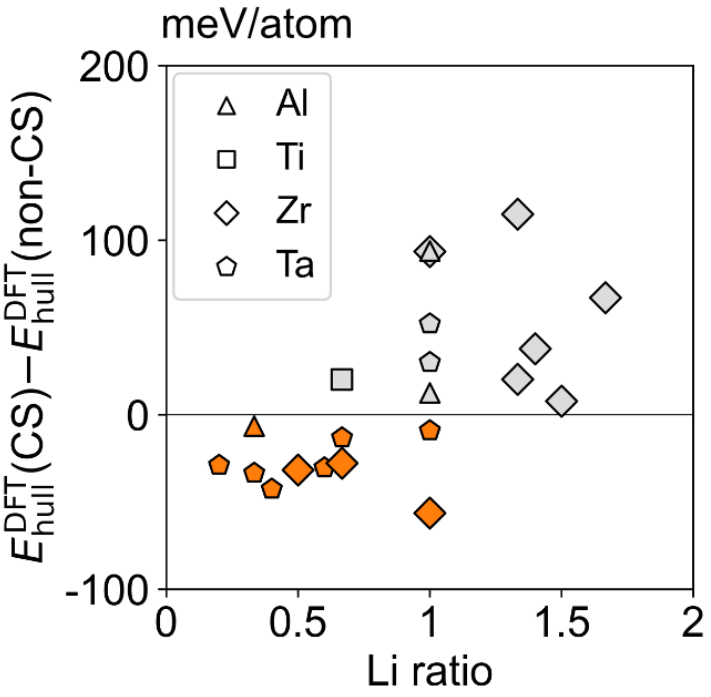

Fig. S6. Relative stability of CS and non-CS frameworks in SPINNER-generated structures. Scatter plot of the E_{hull}^{DFT} (CS) − E_{hull}^{DFT} (non-CS) as a function of Li ratio for each composition. A positive correlation between E_{hull}^{DFT} (CS) − E_{hull}^{DFT} (non-CS) and Li ratio is maintained, and no stable CS-topology structures are found at Li ratios above 1.0.

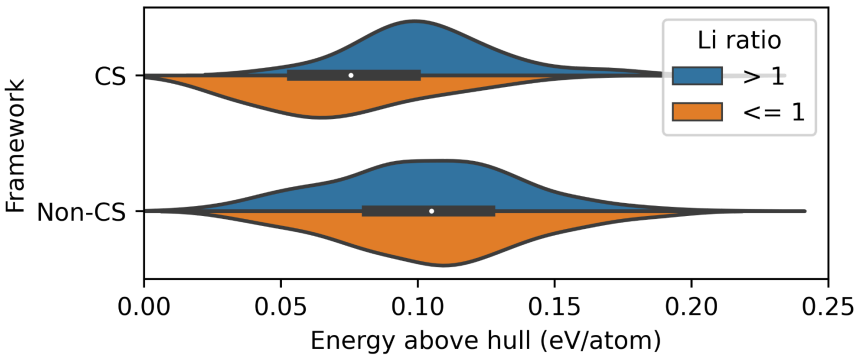

Fig. S7. Energy-above-hull distributions of CS and non-CS frameworks at low and high Li ratios. Violin plots show the stability of CS and non-CS structures, grouped by Li ratio (≤ 1 vs. > 1). Non-CS frameworks exhibit similar stability distributions across both Li-ratio groups, whereas CS frameworks are more stable at low Li ratios and less stable at high Li ratios.

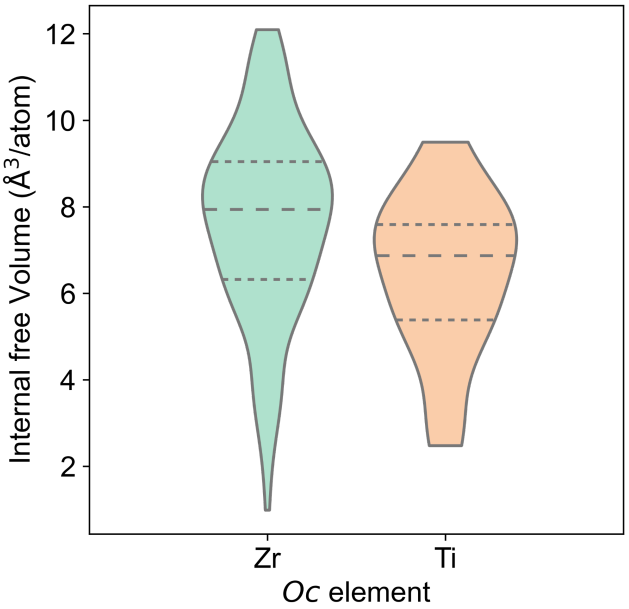

Fig. S8. Internal free-volume distributions in Zr- and Ti-containing frameworks. Violin plots show the distributions of internal free volumes for structures where Zr or Ti occupy octahedral sites. The dashed lines mark the quartiles of each distribution. Frameworks with Zr exhibit systematically larger internal free volumes than those with Ti, consistent with the larger ionic radius of Zr^{4+} (86 pm) compared to Ti^{4+} (75 pm).

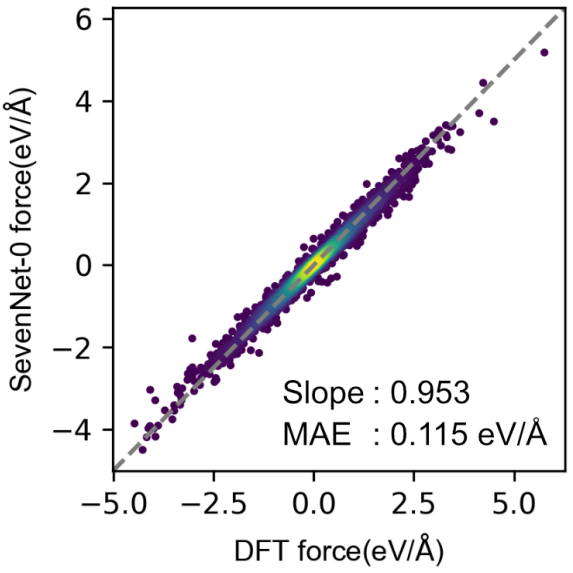

Fig. S9. Validation of force predictions from SevenNet-0. Parity plot comparing MLIP (SevenNet-0)[8] and DFT forces from 1000 K molecular dynamics (MD) trajectories of a test structure, Zn-substituted $LiIn(IO_3)_4$ (Materials Project ID: mp-973966), for which systematic force softening was previously reported.[9] The fitted slope (0.953) and mean absolute error (MAE = 0.115 eV $Å^{-1}$) indicate close agreement with DFT and show no evidence of systematic softening of the potential energy surface.

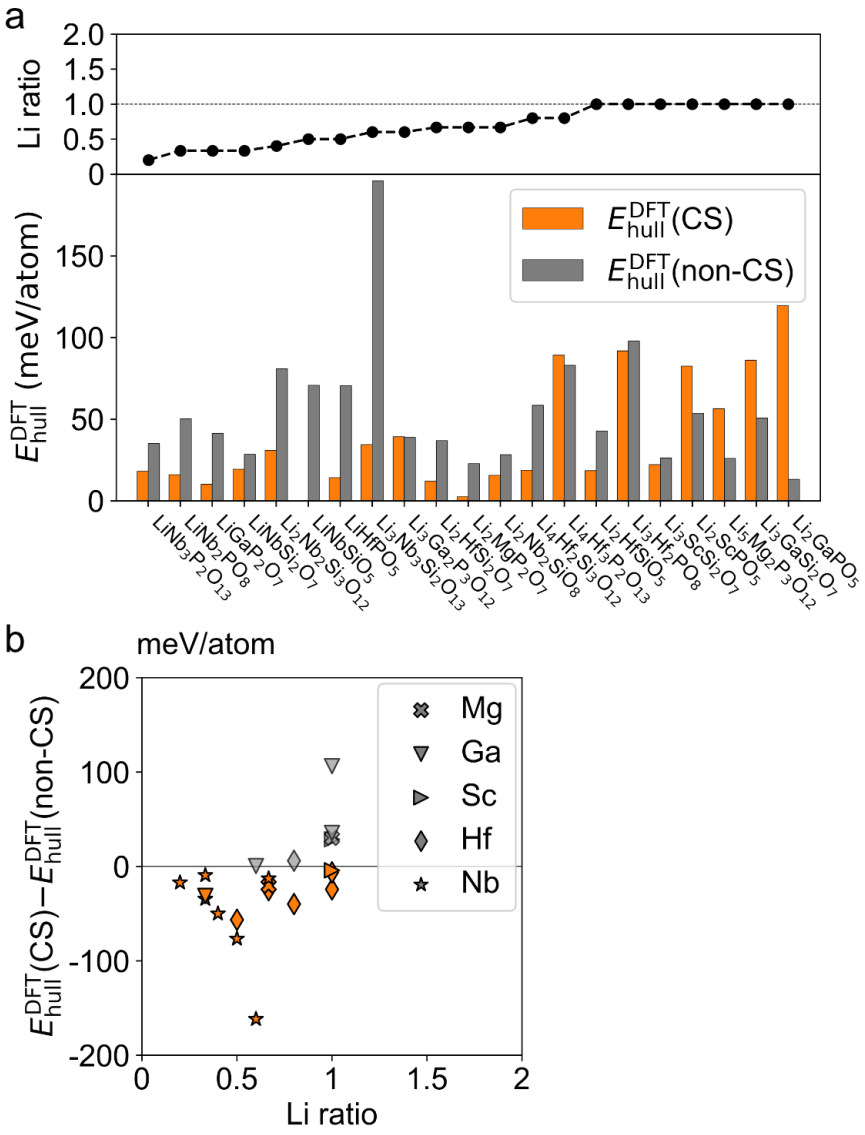

Fig. S10. Stability of CS and non-CS frameworks as a function of Li ratio. (a) DFT hull energies of the lowest-energy CS (orange) and non-CS (gray) structures for each composition. Compositions are ordered first by Li ratio and then by the energy difference between CS and non-CS structures within each ratio group. (b) Scatter plot of E_{hull}^{DFT} (CS) − E_{hull}^{DFT} (non-CS) versus Li ratio for each composition.

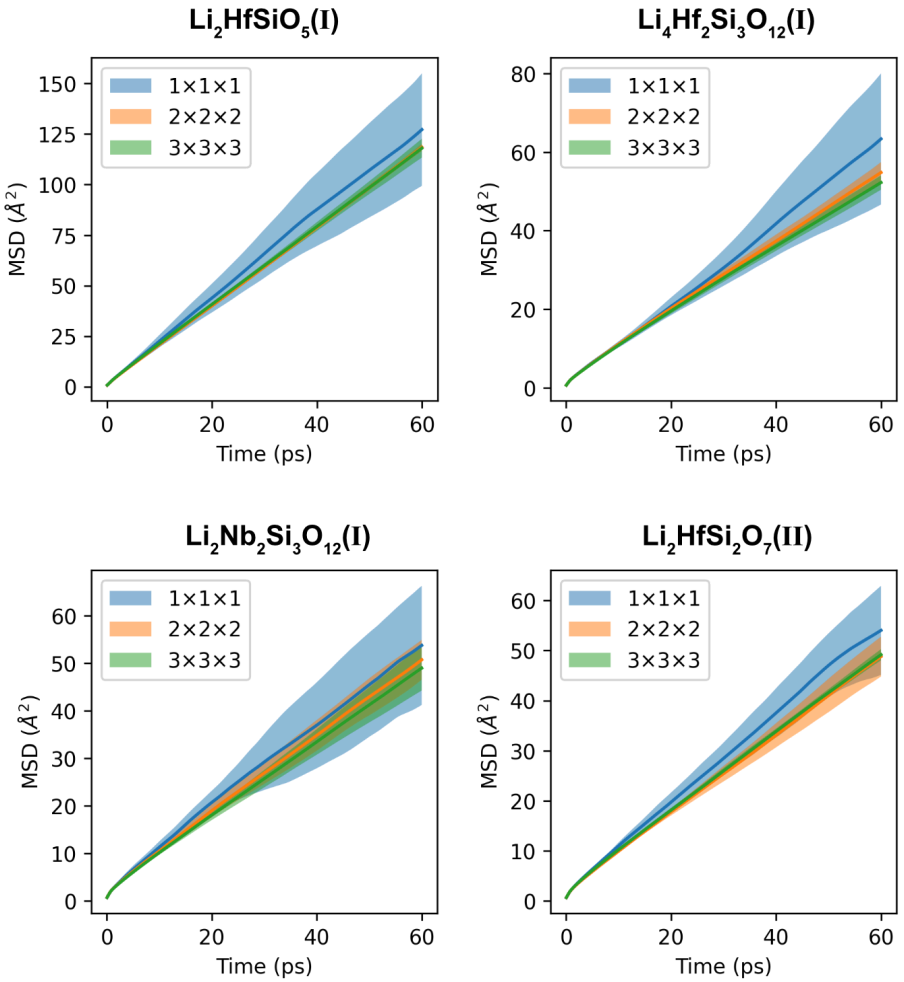

Fig. S11. Cell-size dependence of computed diffusion. Mean-squared displacement (MSD) curves from MD simulations at 1000 K using SevenNet-0 are shown for unit cells, 2×2×2 supercells, and 3×3×3 supercells across representative systems. Colored bands indicate the standard deviation across five independent MSD curves. The results demonstrate negligible finite-size effects in the calculated diffusion coefficients.

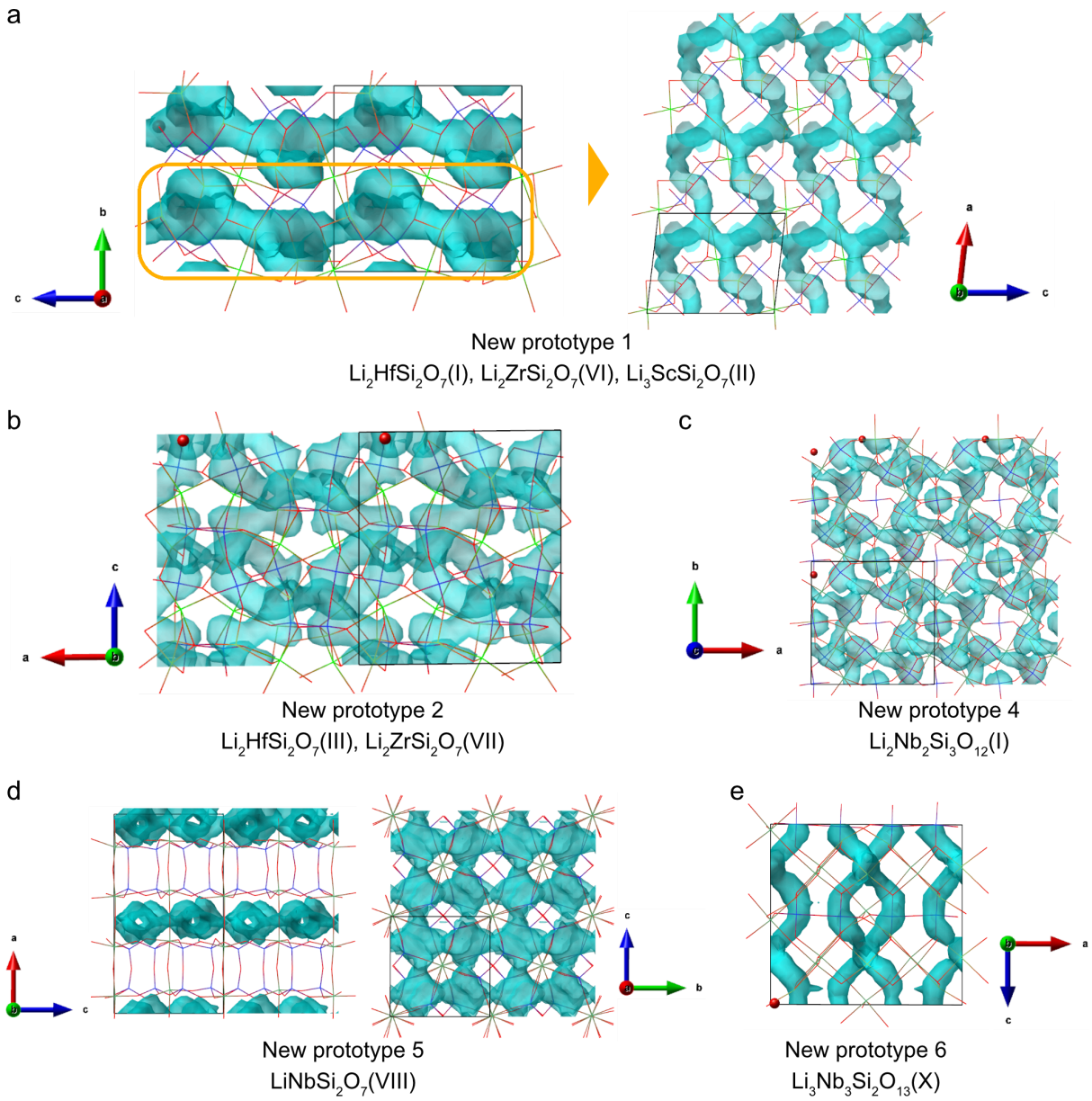

Fig. S12. Li-ion conduction pathways in candidate oxide solid electrolyte structures. Isosurfaces of Li probability density from DFT-MD simulations highlight conduction channels in representative candidates with novel frameworks. (a) Quasi two-dimensional pathways in $Li_2HfSi_2O_7$(I), $Li_2ZrSi_2O_7$(VI), and $Li_3ScSi_2O_7$(II). Left: side view; right: top view (boxed in orange). (b) Three-dimensional pathways in $Li_2HfSi_2O_7$(III) and $Li_2ZrSi_2O_7$(VII). (c) Three-dimensional pathways in $Li_2Nb_2Si_3O_{12}$(I). (d) Quasi two-dimensional pathways in $LiNbSi_2O_7$(VIII). Left: side view; right: top view. (e) Quasi one-dimensional pathways in $Li_3Nb_3Si_2O_{13}$(X).

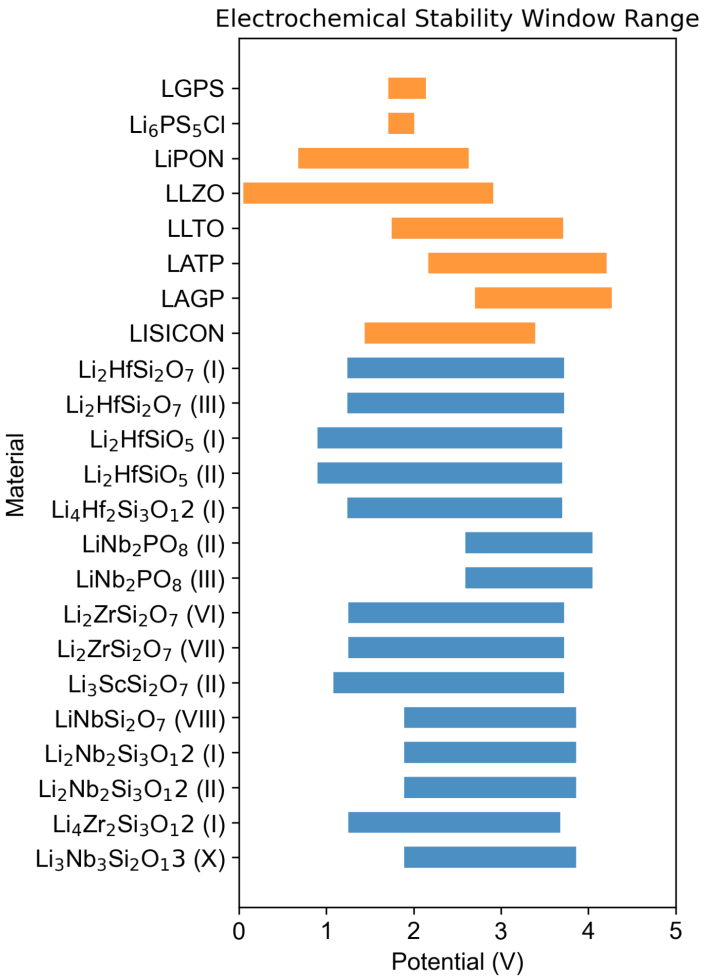

Fig. S13. Electrochemical stability windows (ESW) of candidate SSEs. Blue bars represent the ESW ranges of the candidate SSEs identified in this study, whereas orange bars represent those of previously reported well-known SSEs.[10] The ESWs are evaluated from Li grand potential phase diagrams, with the reduction and oxidation limits defined by the onset potentials at which each phase becomes thermodynamically unstable toward the most favorable decomposition products.

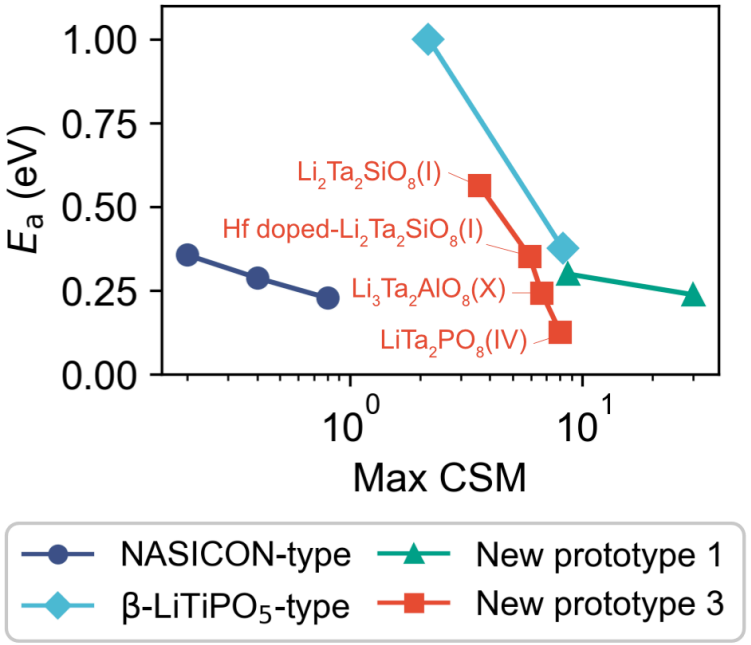

Fig. S14. Relationship between the activation barrier and the Continuous Symmetry Measure (CSM)[11] value for each prototype family. The x-axis value of each marker represents the maximum CSM value among Li sites, and the y-axis value represents the activation barrier. For both axes, each marker corresponds to the average value for compounds sharing the same framework and Li ratio. Across all prototype families, the activation barrier decreases with increasing CSM.

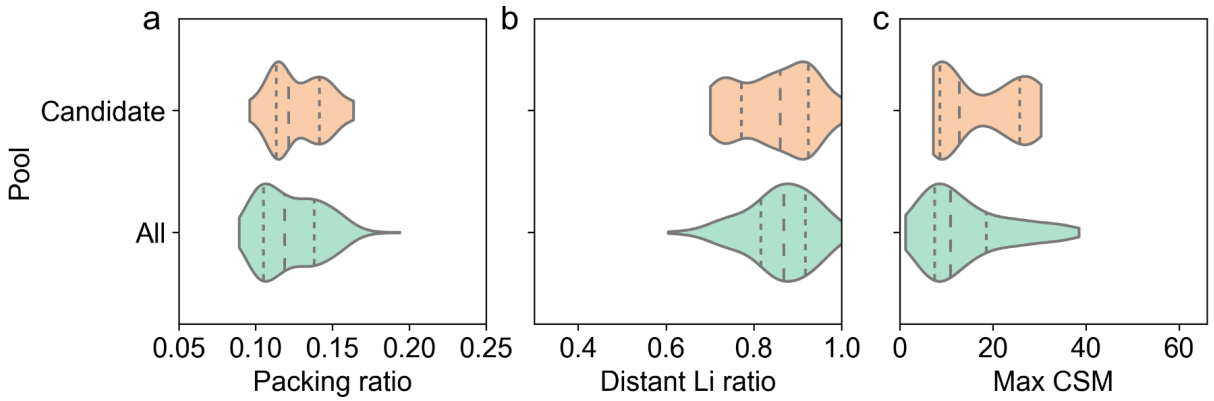

Fig. S15. Structural descriptors comparison. Distributions of structural descriptors for the 438 CS-framework structures generated by TOPIC with $E_{\text{hull}} \leq 50$ meV/atom, compared with those of the 15 high-conductivity candidate structures: (a) polyhedra packing ratio, (b) distant Li-site ratio, and (c) maximum CSM value among Li sites. The 15 high-conductivity candidates are not clearly separated from the full CS-framework set by any single descriptor, although the maximum CSM shows a somewhat more noticeable difference than the other two descriptors.

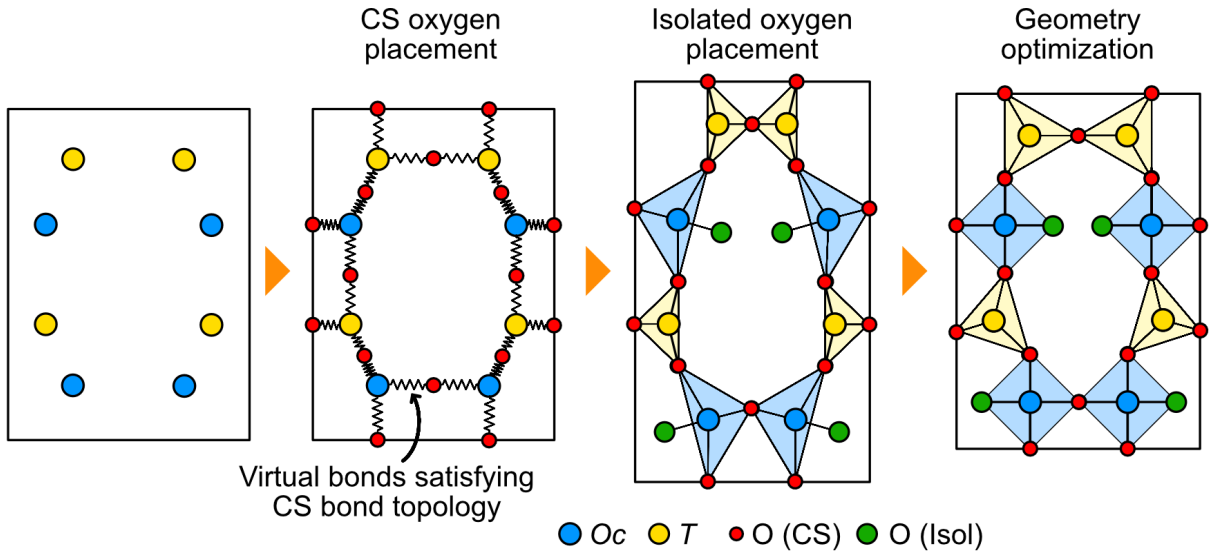

Fig. S16. Schematic illustration of the extension of TOPIC to mixed corner-sharing and isolated-anion frameworks. A virtual bond network satisfying the corner-sharing topology is first constructed between neighboring cations, followed by placement of corner-sharing oxygen atoms on the bonds. Isolated oxygen atoms (or other anions) are then added around undercoordinated cations to satisfy their target coordination environments, and the resulting structure is subsequently refined by geometry optimization.

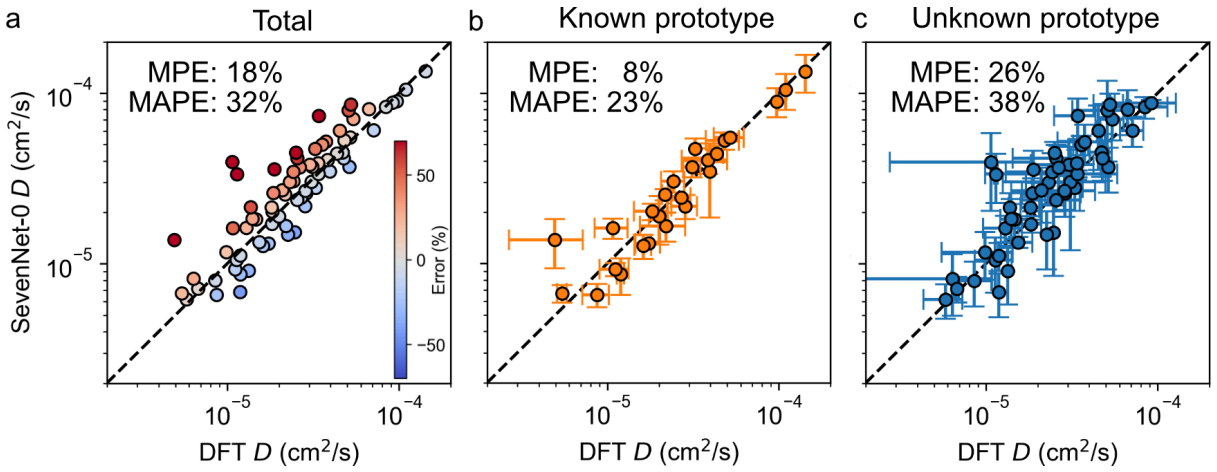

Fig. S17. Comparison of diffusion coefficients predicted by SevenNet-0 and DFT. Diffusion coefficients of the 15 oxide solid electrolyte candidates identified in this study, as predicted by SevenNet-0 and DFT, are compared. (a) Parity plot for all candidates. The color of each point represents the percentage error relative to DFT. (b) Parity plot for materials with known prototype structures (NASICON-, $LiTaSiO_5$-, and β-$LiTiPO_5$-type). (c) Parity plot for materials with novel prototype structures. MPE and MAPE denote the mean percentage error and mean absolute percentage error, respectively. Error bars represent the standard deviation from independent MD runs.

Supplementary Tables.

Table S1. Ionic radii and coordination numbers (CN) used in this study. Shannon ionic radii[13] are listed along with the corresponding coordination numbers. The cation-to-oxygen radius ratio (r_C/r_O) is also presented. According to Pauling's rule,[14] r_C/r_O values of 0.225–0.414 favor tetrahedral coordination (CN = 4), while values of 0.414–0.645 favor octahedral coordination (CN = 6).

Ion	Coordination number	Ionic radius (pm)	r_C/r_O
Mg^{2+}	6	86	0.683
Al^{3+}	4	53	0.421
	6	67.5	0.536
Si^{4+}	4	40	0.317
P^{5+}	4	31	0.246
S^{6+}	4	26	0.206
Sc^{3+}	6	88.5	0.702
Ti^{4+}	6	75	0.595

Ion	Coordination number	Ionic radius (pm)	r_C/r_O
Ga^{3+}	4	61	0.484
	6	76	0.603
Se^{3+}	3	42	0.333
Zr^{4+}	6	86	0.683
Nb^{5+}	6	78	0.619
Te^{6+}	6	70	0.556
Hf^{4+}	6	85	0.675
Ta^{5+}	6	78	0.619

Table S2. Benchmark comparison between TOPIC and SPINNER. Benchmark results for the $LiTi_2P_3O_{12}$, $LiGaSe_2O_6$, β-$LiAlSiO_4$, $LiTiPO_5$, and $LiTaSiO_5$ systems. The table compares the number of times the reference framework was found (N_{found}) in 60,000 generated structures and the total wall time required to generate those structures using TOPIC, SPINNER applied to Li-removed framework structures (denoted as SPINNER (Li-removed)), and SPINNER applied to all-atom structures (denoted as SPINNER (All-atom)).

[a]For $LiTi_2P_3O_{12}$, all-atom SPINNER was unable to complete 60,000 structure generations because the computational cost of further calculations was prohibitively high.

System	Z	TOPIC		SPINNER (Li-removed)		SPINNER (All-atom)	
		N_{found}	Wall time (hours)	N_{found}	Wall time (hours)	N_{found}	Wall time (hours)
$LiTi_2P_3O_{12}$	6	1,524	34.8	68	123.1	-[a]	-[a]
$LiGaSe_2O_6$	8	5	11.9	0	30.6	0	94.7
β-$LiAlSiO_4$	12	2	25.6	0	36.9	0	242.3
$LiTiPO_5$	4	31	2.4	16	8.3	9	12.1
$LiTaSiO_5$	4	15	2.9	4	6.1	3	9.4

Table S3. Comparison of activation energies and ionic conductivities obtained from DFT and SevenNet-0. Activation energies (E_a) and room-temperature ionic conductivities (σ_{300K}) are listed for pristine $LiGa(SeO_3)_2$ and doped systems (Ga-doped $LiTiPO_5$ and P-doped $Li_2Mg_2(SO_4)_3$). SevenNet-0 also reproduces the activation energy of $LiTa_2PO_8$, which was not included in its training set. The results demonstrate that SevenNet-0 predicts both activation energies and conductivities with reasonable accuracy compared to DFT.

System	Reference	E_a (DFT)	E_a (SevenNet-0)	σ_{300K} (DFT)	σ_{300K} (SevenNet-0)
$LiGa(SeO_3)_2$	Ref[12]	0.320 ± 0.070	0.356 ± 0.058	0.212 (0.013, 3.57)	0.057
Ga-doped $LiTiPO_5$	Ref[12]	0.212 ± 0.071	0.267 ± 0.016	1.70 (0.098, 29.7)	0.385
P-doped $Li_2Mg_2(SO_4)_3$	Ref[12]	0.232 ± 0.073	0.227 ± 0.058	2.74 (0.145, 52.0)	3.54
$LiTa_2PO_8$	Ref[15]	0.16	0.160 ± 0.013	35.3	28.85

Table S4. DFT hull energies of CS and non-CS frameworks for 45 target quaternary compositions. For each formula, the Li ratio, E_{hull}^{DFT} (CS), and E_{hull}^{DFT} (non-CS) (in meV atom^{-1}) are listed. The comparison highlights the relative stability of CS versus non-CS frameworks across different Li ratios, supporting the robustness of the Li-ratio descriptor.

Formula	Li ratio	E_{hull}^{DFT} (CS)	E_{hull}^{DFT} (non-CS)	Formula	Li ratio	E_{hull}^{DFT} (CS)	E_{hull}^{DFT} (non-CS)
$LiTa_3P_2O_{13}$	0.200	**19.2**	88.8	$Li_4Zr_2Si_3O_{12}$	0.800	**34.1**	75.2
$LiNb_3P_2O_{13}$	0.200	**18.1**	35.2	$Li_4Hf_2Si_3O_{12}$	0.800	**21.3**	58.6
$LiNb_2PO_8$	0.333	**16.1**	50.3	$Li_4Ti_2Si_3O_{12}$	0.800	61.2	**57.1**
$LiTaSi_2O_7$	0.333	**16.0**	49.4	$Li_4Hf_3P_2O_{13}$	0.800	89.3	**83.1**
$LiGaP_2O_7$	0.333	**10.3**	41.4	$Li_4Zr_3P_2O_{13}$	0.800	100.7	**93.8**
$LiAlP_2O_7$	0.333	**2.1**	27.1	$Li_4Ti_3P_2O_{13}$	0.800	133.5	**79.2**
$LiNbSi_2O_7$	0.333	**19.4**	28.5	Li_2ZrSiO_5	1.000	**26.9**	86.6
$Li_2Ta_2Si_3O_{12}$	0.400	**10.9**	90.7	$Li_3TaAl_2O_7$	1.000	**17.8**	52.9
$Li_2Nb_2Si_3O_{12}$	0.400	**30.9**	80.9	$Li_5Ta_3Al_2O_{13}$	1.000	**58.1**	87.0
$LiNbSiO_5$	0.500	**0**	76.7	Li_2HfSiO_5	1.000	**18.6**	42.8
$LiHfPO_5$	0.500	**14.2**	70.7	Li_2TaAlO_5	1.000	**17.1**	34.0
$LiZrPO_5$	0.500	**26.9**	58.5	$Li_3Ta_2AlO_8$	1.000	**15.2**	26.6
$Li_3Nb_3Si_2O_{13}$	0.600	**34.5**	196.1	$Li_3Hf_2PO_8$	1.000	**91.8**	97.9
$Li_3Ta_3Si_2O_{13}$	0.600	**35.3**	86.2	$Li_3ScSi_2O_7$	1.000	**22.3**	26.3
$Li_3Al_2P_3O_{12}$	0.600	**43.2**	60.6	$Li_3AlSi_2O_7$	1.000	57.2	**44.7**
$Li_3Ga_2P_3O_{12}$	0.600	39.3	**38.9**	$Li_5Ta_2Al_3O_{12}$	1.000	71.2	**56.4**
$Li_2ZrSi_2O_7$	0.667	**25.9**	58.8	$Li_3Zr_2PO_8$	1.000	135.3	**114.5**
$Li_2HfSi_2O_7$	0.667	**12.1**	37.0	Li_2ScPO_5	1.000	82.5	**53.6**
$Li_2MgP_2O_7$	0.667	**2.6**	22.8	$Li_5Mg_2P_3O_{12}$	1.000	56.6	**26.1**
$Li_2Ta_2SiO_8$	0.667	**17.9**	32.8	$Li_3GaSi_2O_7$	1.000	86.1	**50.7**
$Li_2Nb_2SiO_8$	0.667	**15.6**	28.3	Li_2AlPO_5	1.000	122.6	**28.7**
$Li_2TiSi_2O_7$	0.667	45.0	**29.4**	Li_2GaPO_5	1.000	119.5	**13.2**
				$Li_3Ti_2PO_8$	1.000	-	**69.8**

Table S5. Frequently occurring frameworks identified in the comprehensive screening. Listed are representative chemical formulas and their activation energies (E_a), grouped by framework type and Li ratio. Experimental E_a values for $LiTi_2(PO_4)_3$ and $LiTiPO_5$ are taken from the literature.[16–20]

Framework type	Li ratio	Formula	E_a (eV)	Reference
NASICON-type	0.2	$LiTi_2(PO_4)_3$	0.30~0.46	Ref.[16–19]
	0.4	$Li_2Nb_2Si_3O_{12}$	0.267	-
		$Li_2Ta_2Si_3O_{12}$	0.306	-
	0.8	$Li_4Hf_2Si_3O_{12}$	0.183	-
		$Li_4Zr_2Si_3O_{12}$	0.270	-
β-$LiTiPO_5$-type	0.5	$LiTiPO_5$	1.00	Ref.[20]
	1.0	Li_2HfSiO_5	0.375	-
New prototype 1	0.667	$Li_2ZrSi_2O_7$	0.277	-
		$Li_2HfSi_2O_7$	0.319	-
	1.0	$Li_3ScSi_2O_7$	0.236	-
New prototype 3	0.333	$LiTa_2PO_8$	0.125	-
	0.667	$Li_2Ta_2SiO_8$	0.562	-
	1.0	$Li_3Ta_2AlO_8$	0.242	-

Table S6. Continuous Symmetry Measure (CSM) analysis[11] of Li environments. CSM values are reported for Li ions in octahedral and tetrahedral sites across β-$LiTiPO_5$-, NASICON-, and new prototype 1 frameworks. Larger CSM values indicate greater deviations from ideal site symmetry, reflecting the structural distortions induced by Li stuffing.

Prototype	Formula	Octahedral site CSM	Tetrahedral site CSM
β-$LiTiPO_5$ type	$LiTiPO_5$	2.2	-
	Li_2HfSiO_5	-	5.4, 8.2
NASICON type	$LiTi_2P_3O_{12}$	5.0	-
	$Li_2Ta_2Si_3O_{12}$	23.0 ~ 24	10.6 ~ 15.1
	$Li_2Nb_2Si_3O_{12}$	24.1	13.7
	$Li_4Hf_2Si_3O_{12}$	19.4	1.8 ~ 23.3
	$Li_4Zr_2Si_3O_{12}$	27.5	1.4 ~ 3.1
New prototype 1	$Li_2HfSi_2O_7$	-	1.8, 8.7
	$Li_2ZrSi_2O_7$	-	1.5, 8.6
	$Li_3ScSi_2O_7$	11.1	1.6 ~ 30.0

References.

1 S. Kang, W. Jeong, C. Hong, S. Hwang, Y. Yoon and S. Han, *npj Comput. Mater.*, 2022, **8**, 108.
2 C. Hong, J. M. Choi, W. Jeong, S. Kang, S. Ju, K. Lee, J. Jung, Y. Youn and S. Han, *Phys. Rev. B*, 2020, **102**, 224104.
3 Y. Han, C. Ding, J. Wang, H. Gao, J. Shi, S. Yu, Q. Jia, S. Pan and J. Sun, *Nat. Comput. Sci.*, 2025, **5**, 255–267.
4 G. Bergerhoff, R. Hundt, R. Sievers and I. D. Brown, *J. Chem. Inf. Comp. Sci.*, 1983, **23**, 66–69.
5 V. L. Deringer, A. L. Tchougréeff and R. Dronskowski, *J. Phys. Chem. A*, 2011, **115**, 5461–6.
6 J. Kim, J. Kim, M. Avdeev, H. Yun and S.-J. Kim, *J. Mater. Chem. A*, 2018, **6**, 22478–22482.
7 A. Jain, S. P. Ong, G. Hautier, W. Chen, W. D. Richards, S. Dacek, S. Cholia, D. Gunter, D. Skinner, G. Ceder and K. A. Persson, *Apl. Mater.*, 2013, **1**, 011002.
8 Y. Park, J. Kim, S. Hwang and S. Han, *J. Chem. theory Comput.*, 2024, **20**, 4857–4868.
9 B. Deng, Y. Choi, P. Zhong, J. Riebesell, S. Anand, Z. Li, K. Jun, K. A. Persson and G. Ceder, *npj Comput. Mater.*, 2025, **11**, 9.
10 Y. Zhu, X. He and Y. Mo, *ACS Appl. Mater. Interfaces*, 2015, **7**, 23685–23693.
11 D. D. Stefano, A. Miglio, K. Robeyns, Y. Filinchuk, M. Lechartier, A. Senyshyn, H. Ishida, S. Spannenberger, D. Prutsch, S. Lunghammer, D. Rettenwander, M. Wilkening, B. Roling, Y. Kato and G. Hautier, *Chem*, 2019, **5**, 2450–2460.
12 K. Jun, Y. Sun, Y. Xiao, Y. Zeng, R. Kim, H. Kim, L. J. Miara, D. Im, Y. Wang and G. Ceder, *Nat. Mater.*, 2022, **21**, 924–931.
13 R. D. Shannon, *Acta Crystallogr. Sect. A*, 1976, **32**, 751–767.
14 L. Pauling, *J. Am. Chem. Soc.*, 1929, **51**, 1010–1026.
15 F. Hussain, P. Li and Z. Li, *J. Phys. Chem. C*, 2019, **123**, 19282–19287.
16 Y. Luo, X. Liu, C. Wen, T. Ning, X. Jiang and A. Lu, *Appl. Phys. A*, 2023, **129**, 518.
17 K. Takada, M. Tansho, I. Yanase, T. Inada, A. Kajiyama, M. Kouguchi, S. Kondo and M. Watanabe, *Solid State Ion.*, 2001, **139**, 241–247.
18 K. Arbi, M. A. París and J. Sanz, *J. Phys. Chem. B*, 2006, **110**, 6454–6457.
19 H. Aono, E. Sugimoto, Y. Sadaoka, N. Imanaka and G. Adachi, *Solid State Ion.*, 1991, **47**, 257–264.
20 A. Robertson, J. G. Fletcher, J. M. S. Skakle and A. R. West, *J. Solid State Chem.*, 1994, **109**, 53–59.